Journal of Solid State Chemistry **145,** 678–693 (1999)
Article ID jssc.1999.8285, available online at http://www.idealibrary.com on IDEAL®

Cation-Deficient Perovskite-Related $(Ba, La)_nTi_{n-\delta}O_{3n}$ ($n \geq 4\delta$) Microphases in the $La_4Ti_3O_{12}$–$BaTiO_3$ System: An HRTEM Approach

G. Trolliard,[1] N. Harre, D. Mercurio, and B. Frit

Sciences des Procédés Céramiques et de Traitements de Surface, UMR-CNRS 6638, Faculté des Sciences, 123, Avenue Albert Thomas, 87060 Limoges Cedex, France

Received September 21, 1998; in revised form March 12, 1999; accepted March 23, 1999

The large nonstoichiometric domain, observed in the $La_4Ti_3O_{12}$-rich part of the $La_4Ti_3O_{12}$–$BaTiO_3$ system, has been shown to correspond to a continuous series of cation-deficient perovskite-related $(Ba, La)_nTi_{n-\delta}O_{3n}$ ($n \geq 4\delta$) microphases. The crystal structures of these microphases have been analyzed by electron diffraction and high-resolution electron microscopy. They can be described as coherent intergrowths of *P*-perovskite-like blocks $La_4Ti_3O_{12}$ and *Q*-perovskite-like blocks $BaLa_4Ti_4O_{15}$, respectively, constitutive of the simple basic terms $n = 4$ and $n = 5$ of the previously identified $(Ba, La)_nTi_{n-1}O_{3n}$ series. The corresponding $Ba_QLa_{4(P+Q)}Ti_{3P+4Q}O_{12P+15Q}$ microphases can thus be denoted by 4^P5^Q in a compact form. In fact, only the 4^P5^1 intergrowth sequences have been observed. Eight of these are clearly shown by direct imaging. No intergrowth terms were observed for compositions ranging from $BaLa_4Ti_4O_{15}$ ($n = 5$) to $Ba_2La_4Ti_5O_{18}$ ($n = 6$). The ability of the system to develop coherent intergrowths has been discussed in the light of information provided by an accurate analysis of crystal structures of the basic members of the series: $La_4Ti_3O_{12}$ ($n = 4$), $BaLa_4Ti_4O_{15}$ ($n = 5$), and $Ba_2La_4Ti_5O_{18}$ ($n = 6$). © 1999 Academic Press

Key Words: **intergrowths; HRTEM; cation-deficient perovskite; dielectric materials.**

INTRODUCTION

Complex oxides with cation-deficient perovskite-related structures and the general formula $A_nB_{n-1}O_{3n}$ ($n \geq 3$) have been synthesized in numerous systems with A = Ca, Sr, Ba, La and $B = M^{II}$(Mg, Zn, Cd, Ni, Co), M^{III} (B, Fe, Ti), M^{IV} (Ti, Ru), M^{V} (Nb, Ta), and M^{VI} (W, Re) (1–21). Most of them are part of a homologous series of trigonal structures which can be described as being derived from the perovskite structure by the periodic introduction of intrinsic stacking faults in the cubic close packing of AO_3 mixed layers. In these structures, slabs of normal cubic perovskite are intergrown with regions stacked in hexagonal close packing of the type found in the hexagonal perovskite $BaNiO_3$. The change in composition from the ideal ABO_3 is brought about by layers of empty octahedra in the center of the hexagonal slabs, which could be filled with B cations in the stoichiometric perovskite. For a given composition $A_nB_{n-1}O_{3n}$ ($n \geq 3$), the number of AO_3 mixed layers in each perovskite slab is n, and that of occupied B layers is $(n - 1)$. Bontchev *et al.* (15) and Van Tandeloo *et al.* (19) have shown, in the case of the $La_4Ti_3O_{12}$–$LaTiO_3$ system, that slabs of different thicknesses ($n = 4$ and 5 or $n = 5$ and 6, for example) can be coherently intergrown to constitute a more general series $La_nTi_{n-\delta}O_{3n}$ ($n \geq 4\delta$; $\delta \geq 1$) of complex commensurate or incommensurate superstructures (complex perovskite-related polytypoids). Six different ordered stacking sequences have been observed by electron microscopy direct imaging. Some disordered intergrowths of simple members ($5 \leq n \leq 7$) of the $Sr_n(Nb, Ti)_{n-1}O_{3n}$ series have recently been found in the $Sr_5Nb_4O_{15}$–$SrTiO_3$ line of the SrO–Nb_2O_5–TiO_2 system (22).

We asked the question whether similar intergrowths could exist when two kinds of cations A, which are very different in size, are present. In response, we decided to reinvestigate the $La_4Ti_3O_{12}$–$BaTiO_3$ system previously studied by Saltykova *et al.* (1). As shown by the equilibrium phase diagram proposed (Fig. 1), they found only the simplest members, $n = 4$, 5, 6, and 8 of the $(Ba, La)_nTi_{n-1}O_{3n}$series. In fact, and contrary to these first results, coherent intergrowths of $n = 4$ and $n = 5$ simple basic members do exist and we have synthesized them (23, 24). They will be described in the second part of this paper. In contrast, no intergrowth was observed for the $n = 5$ and $n = 6$ basic members. This problem will be discussed in the last part of our paper. A good understanding of the structural stability of such superstructures requires a detailed analysis of the crystal structures of their basic building units, i.e., of the simple members ($n = 4$, 5, 6) of the $(Ba, La)_nTi_{n-1}O_{3n}$ series. Since previous studies did not give sufficient information in terms of oxygen atom coordinates and the possible cation ordering, we have undertaken the

[1] To whom correspondence should be addressed.

0022-4596/99 $30.00

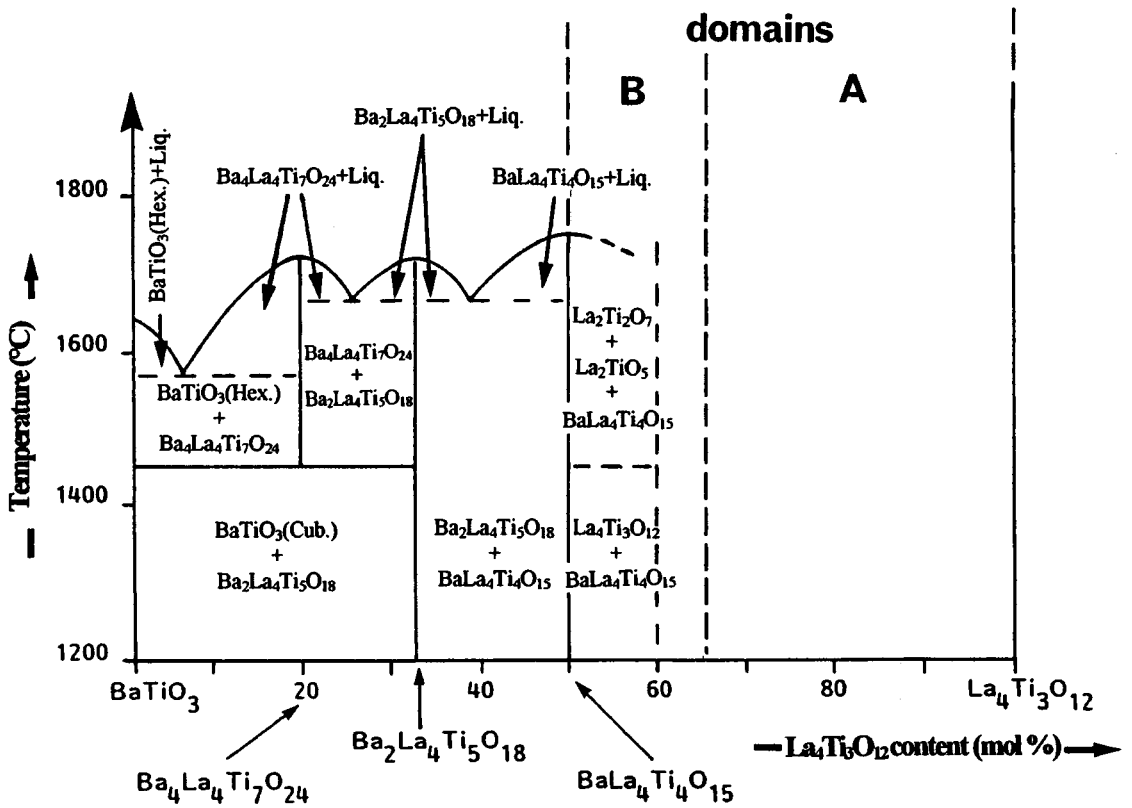

FIG. 1. Equilibrium phase diagram in the $La_4Ti_3O_{12}$–$BaTiO_3$ system, according to Saltykova *et al.* (1).

determination of the crystal structure of these three compounds. The first part of the paper is devoted to a detailed and comparative description of the structure of the three structures.

STRUCTURAL CONSIDERATIONS ON THE MEMBERS $n = 4$, 5, AND 6 OF THE $(Ba, La)_nTi_{n-1}O_{3n}$ SERIES

The main crystal data of these phases are given in Table 1. The detailed results concerning the $n = 6$ member, $Ba_2La_4Ti_5O_{18}$, and the $n = 5$ member, $BaLa_4Ti_4O_{15}$, were obtained from single-crystal X-ray diffraction experiments and have already been published (25, 26). Those concerning the $n = 4$ member, $La_4Ti_3O_{12}$, correspond to a Rietveld full profile analysis of a neutron powder diffraction pattern registered on the D2B instrument, at ILL (Grenoble, France). They will be published elsewhere. They are accurate enough to be significantly compared to the others. The refined atomic coordinates and thermal parameters are reported in Table 2.

The three structures correspond to a close packing of AO_3 mixed layers. Within the layers the A and O atoms are ordered in the way shown in Fig. 2a. Each A atom is surrounded by six oxygen atoms, whereas each oxygen atom has two A atoms linearly coordinated to it among its six nearest neighbors. To avoid any direct A–A connection, successive layers are shifted one from another by $1/3\langle 01\bar{1}0\rangle_H$vectors, so that A atom positions in one layer project in the center of a triangle formed by the A atoms in the adjacent layers (position 1 or 2 in Fig. 2a). One quarter of the octahedral interstices between two such layers are surrounded exclusively by oxygen atoms. They are occupied by titanium atoms (small open circles on Figs. 2b–2d). The a_H parameter is determined by the hexagonal sublattice of A atoms and remains nearly constant (≈ 5.6 Å) for each structure. In contrast, the c_H parameter which depends on the stacking sequence of AO_3 layers strongly changes from one structure to the other (Table 1). We can see the three stacking sequences in Fig. 3. All oxygen octahedra located within the cubic-close-packed (ccp) part of the sequence are corner-sharing and occupied by titanium atoms. In each triplet of face-sharing octahedra, characteristic of the hexagonal-close-packed (hcp) part of the sequence, the central octahedra are vacant. As a consequence, in each structure, identical perovskite-like slabs of n AO_3 layers are separated by titanium vacancy layers, each slab being shifted from its neighbor by a $1/3\langle 01\bar{1}0\rangle_H$ vector. Van Tandeloo *et al.* (19) have shown that if the number n is a multiple of 3 -1, the

TABLE 1
Main Crystallographical Characteristics of the First Three Members of the $(Ba, La)_nTi_{n-1}O_{3n}$ Series

	$Ba_2La_4Ti_5O_{18}$ $n = 6$	$BaLa_4Ti_4O_{15}$ $n = 5$	$La_4Ti_3O_{12}$ $n = 4$
Space group	$R\bar{3}$	$P\bar{3}c1$	$R\bar{3}$
Unit cell parameters	$a = 5.584(1)$ $c = 41.176(8)$	$a = 5.5720(10)$ $c = 22.500(2)$	$a = 5.55086(3)$ $c = 26.17799(19)$
Polytypoid symbol	18R	10H	12R
Z	3	2	3
Refinement method	Single-crystal X-ray diffraction data (25)	Single-crystal X-ray diffraction data (26)	Rietveld analysis of neutron powder diffraction pattern (this work)
Reliability factors	$R_1 = 0.0285$ $wR_2 = 0.0671$	$R_1 = 0.0336$ $wR_2 = 0.0777$	$R_B = 2.32\%$ $R_P = 8.48\%$ $R_{WP} = 9.09\%$ $\chi^2 = 2.11\%$ GOF index = 1.4

resulting stacking has a repeat period, along the direction normal to the layers, which contains a single perovskite-like block, and the Bravais system is hexagonal. If the number n is a multiple of 3, or a multiple of $3 + 1$, the stacking only repeats after three blocks and the Bravais system is rhombohedral. Indeed, as we can see in Table 1 and in Fig. 3, the space group is $R\bar{3}$ for $La_4Ti_3O_{12}$ ($n = 4$) and $Ba_2La_4Ti_5O_{18}$ ($n = 6$) with the respective stacking sequences ABCBCABAB… or $(chhc)_3$ (12R polytypoid) and ABCBCABCACABCABABC… or $(chhccc)_3$ (18R polytypoid), whereas the space group is $P\bar{3}c1$ for $BaLa_4Ti_4O_{15}$ ($n = 5$) with the stacking sequence ABCB′C′A′B′C′BC… or $(chhcc)_2$ ($2 \times 5H = 10H$ polytypoid). For $BaLa_4Ti_4O_{15}$, the doubling of the expected stacking sequence is, as we will see below, the consequence of a cooperative tilting of TiO_6 octahedra within the perovskite blocks (A, B, and C not exactly superposed with A′, B′, and C′ AO_3 layers in Fig. 3).

TABLE 2
Refined Positional and Thermal Parameters of $La_4Ti_3O_{12}$

	Position	x	y	z	B (Å^2)
La(1)	6(c)	0	0	0.13401(7)	0.49(3)
La(2)	6(c)	2/3	1/3	0.04559(9)	0.35(2)
Ti(1)	6(c)	0	0	0	0.05(5)
Ti(1)	3(a)	1/3	2/3	0.09149(15)	0.63(6)
O(1)	18(f)	0.56639(30)	0.00711(36)	0.12225(6)	0.53(2)
O(2)	18(f)	0.22089(30)	0.88808(28)	0.04119(8)	0.62(2)

Note. The e.s.d.'s are given as the last digit in parentheses.

In more detail, and for a good understanding of the complex superstructures described in the last section, two main features, mainly concerning the cation sublattice on the one hand and the anion sublattice on the other hand, are worth pointing out.

Cationic Sublattice

The anion and cation sublattices within each perovskite block are, electrostatically speaking, respectively under tension and under compression because of the cation deficiency at the center of the hcp part of each structure. The resulting strain energy is relieved in each structure by a cooperative movement visualized, in the case of the $Ba_2La_4Ti_5O_{18}$ compound, by vertical arrows in Fig. 3a.

An important consequence of this uniaxial distortion is that all the AO_{12} "twinned cuboctahedra," characteristic of the hcp part of the structure, are strongly expanded with respect to the normal ones, characteristic of the perovskite slabs (25,26). It is therefore highly probable that these "twinned cuboctahedra" are preferentially occupied by Ba atoms when Ba and La atoms are both present in the structure. This ordering is all the more probable since it is the simplest way to minimize the electrostatic repulsion that would generate the short A–A distances created in the hcp part of the structure by both the $1/3\langle 01\bar{1}0\rangle_H$ shift of successive perovskite blocks and the cation displacement along the c-direction.

A second consequence of the cationic relaxation is the reconstitution of the body-centered cubic (bcc) cationic subcell characteristic of the ideal perovskite structure (in fact, a CsCl-type subcell) which was destroyed by the $1/3\langle 01\bar{1}0\rangle_H$ shift ($1/3\langle 2\bar{1}\bar{1}\rangle_C$ in the perovskite cell) of perovskite slabs. As we can see in Fig. 4a and 4b, the $1/3$ $[01\bar{1}0]_H$ shift brings the A atoms of a shifted perovskite block to the center of the trigonal faces of the TiO_6 octahedra of the adjacent perovskite slab. The A–Ti distances thus created are too short and so unacceptable. Consequently, the Ti atoms disappear, justifying the cation deficiency with respect to the ideal perovskite. The corresponding vacancies are eliminated by the cation relaxation and a slightly distorted bcc cationic subcell is reconstituted (Fig. 4c). It should therefore be noted that if it is convenient to describe these perovskite-related structures as consisting of perovskite slabs separated by cation vacancy layers, such vacancies in fact do not exist with respect to the ideal perovskite structure. They are purely formal, and the persistence of a bcc cationic subcell is surely the key factor for the stability of these structures.

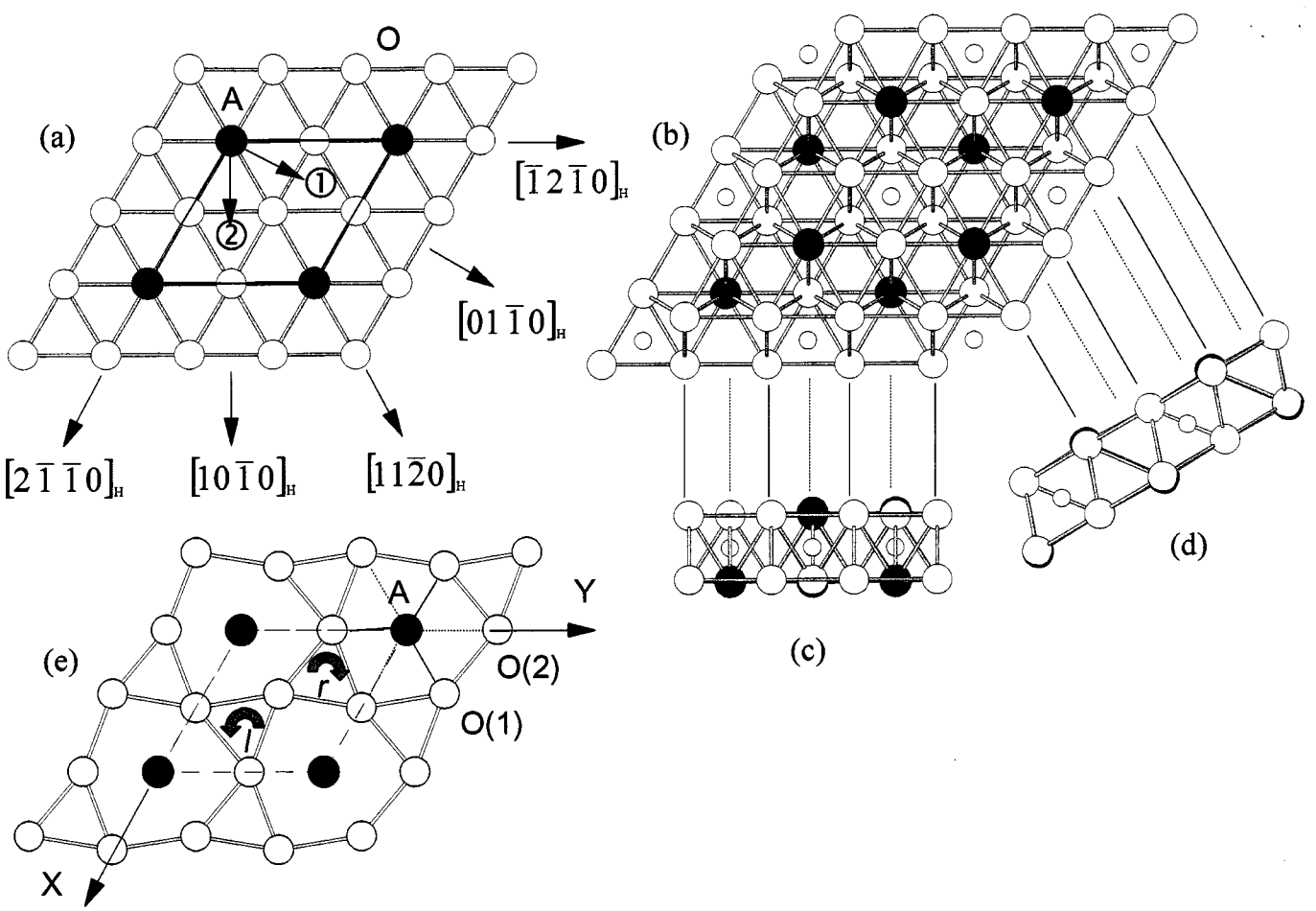

FIG. 2. Schematic views of the AO_3 mixed layers packing in $(Ba,La)_nTi_{n-1}O_{3n}$ ($n = 4$, 5, and 6) basic members: (a) Arrangement of A and O atoms in the AO_3 mixed layers. (b) Stacking of two adjacent AO_3 layers showing the TiO_6 octahedra. (c) View of this stacking along $[10\bar{1}0]_H$, an equivalent direction of the $\langle 01\bar{1}0\rangle_H$ form. (d) View of this stacking along $[11\bar{2}0]_H$, an equivalent direction of the $\langle 2\bar{1}\bar{1}0\rangle_H$ form. (e) The distorted AO_3 layers observed in the $La_4Ti_3O_{12}$ and $BaLa_4Ti_4O_{15}$ structures. r and l visualize respectively the clockwise and counterclockwise rotation of corner-sharing octahedra.

Anionic Sublattice

The oxygen sublattice, within each AO_3 mixed layer, remains perfectly planar and is almost regular for the three structures. The O–O distances are not very different from the average value ($\langle O\text{–}O\rangle \approx 2.8$ Å). In fact, the oxygen sublattice is perfectly regular for the $Ba_2La_4Ti_5O_{18}$ structure (Fig. 2a), but it is slightly distorted for the two other members ($La_4Ti_3O_{12}$ and $BaLa_4Ti_4O_{15}$) as can be seen in Fig. 2e. The A cation lattice remains perfectly hexagonal in the three structures.

The oxygen sublattice distortion corresponds to a cooperative rotation of all the TiO_6 octahedra around the c axis. As shown in Fig. 2e, 3b, and 3c, TiO_6 octahedra which share corners within a perovskite block rotate in opposite senses (r and l in Figs. 2e, 3b, and 3c) from one layer to the other, whereas they rotate in the same sense in the hcp part of the structure. In the $BaLa_4Ti_4O_{15}$ structure, two successive perovskite blocks (the ABCAB sequence and the A′B′C′A′B′ sequence in Fig. 3b) give a global reverse rotation. The c-parameter is then doubled compared to that observed for example in the $Ba_5Ta_4O_{15}$ homologous phase (11,12) for which the oxygen sublattice is not distorted (see Table 3: the space group is $P\bar{3}m1$ instead of $P\bar{3}c1$ for $BaLa_4Ti_4O_{15}$). The global reverse rotation allows the coordination of the A cation to be decreased from [12] to [6 + 3], without distorting the TiO_6 octahedra, when the average cation size is reduced (see Table 3). This cooperative rotation of the TiO_6 octahedra, noted $a^-a^-a^-$ in the Glazer tilt systems (27), is observed in perovskite-related structures as soon as the Goldschmidt tolerance factor t (28) is less than 1 (see Table 3). This doubling of the c-parameter

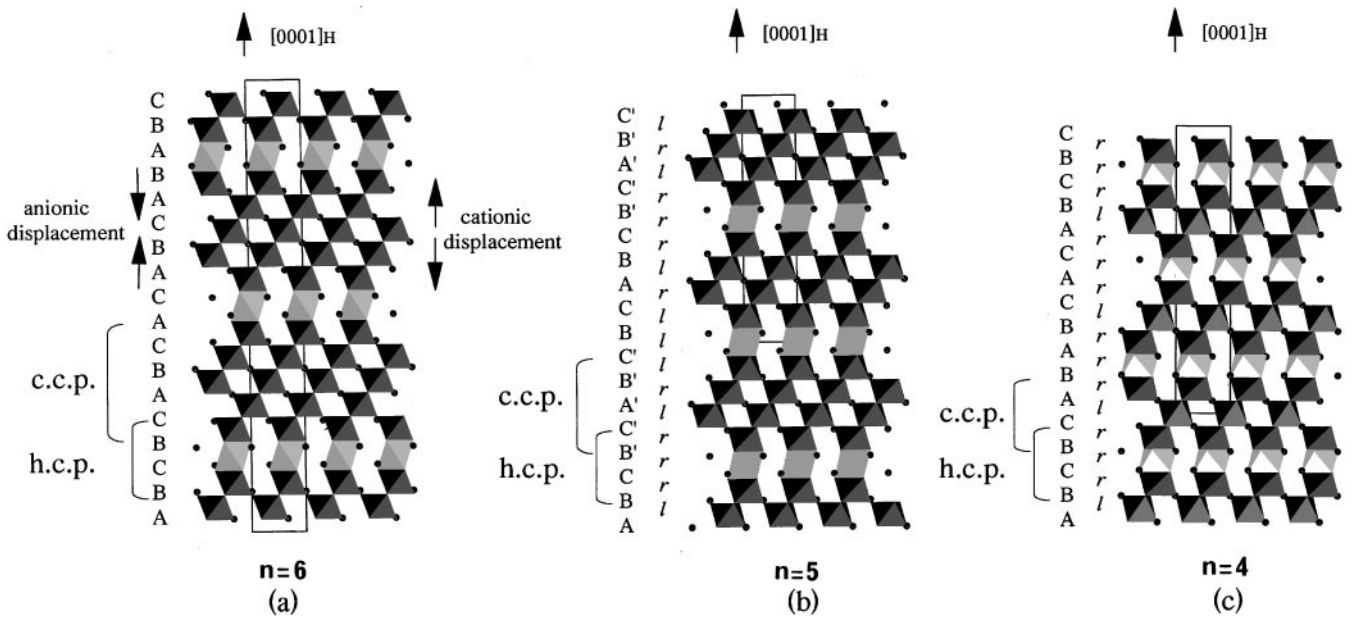

FIG. 3. Schematic representation of $(Ba,La)_nTi_{n-1}O_{3n}$ ($n = 4$, 5, and 6) member structures as viewed along $[2\bar{1}\bar{1}0]_H$. The rotations of TiO_6 octahedra around the c axis are represented by r = clockwise and l = counterclockwise.

resulting from the global reverse rotation can occur only if the number $(n - 1)$ of Ti layers is even (19), which is the case for the $BaLa_4Ti_4O_{15}$ structure ($(n - 1) = 4$).

$(Ba,La)_nTi_{n-\delta}O_{3n}$ INTERGROWTH MICROPHASES

Experimental

The chemical composition of the samples was adjusted to form various intergrowths of stable basic members $n = 4$, 5, and 6 of the $(Ba,La)_nTi_{n-\delta}O_{3n}$ homologous series. All the samples were prepared by a solid-state reaction, under an air atmosphere, of high-purity (more than 99%) commercial La_2O_3, TiO_2, and $BaCO_3$. Appropriate amounts of these starting products were carefully mixed and ground in an agate mortar and calcinated in an alumina crucible at 1200°C for 12 h. After an intermediate grinding the resulting powders were pressed into pellets. These pellets were then sintered at temperatures ranging from 1450 to 1600°C for 24 h. Because of the very high melting temperature of these compounds, perfect long-range ordering of microphases is difficult to reach, and longer annealing time (up to 60 h) was often required. The efficiency of the heat treatment was ascertained by the shape of diffraction spots (stretching along the c^* direction must not be observed) in the selected area electron diffraction (SAED) patterns obtained by electron diffraction.

Bulk structural analysis was carried out by X-ray powder diffraction (XRPD) using a Siemens D5000 diffractometer and Cu$K\alpha$ radiation.

High-resolution transmission electron microscope (HRTEM) observations were performed with a JEOL 2010 microscope operating at 200 kV with a point resolution of 2.3 Å. The specimens consisted of freshly crushed samples deposited on copper grids covered with very thin and holey carbon films. The simulated images were computed using the EMS suite of multislice programs (29), with a spherical aberration constant of 1 mm, focus spread of 10 nm, beam divergence semiangle of 1 mrad, and objective aperture diameter of 14.4 nm^{-1}.

Results and Structural Approach

No microphases resulting from coherent intergrowth of $n = 5$ and $n = 6$ members could be synthesized under our experimental conditions. Whatever the thermal treatment the XRPD patterns of the samples studied systematically corresponded to mixtures of $Ba_2La_4Ti_5O_{18}$ and $BaLa_4Ti_4O_{15}$ phases.

On the other hand, the XRPD patterns of samples whose composition ranges from $n = 4$ ($La_4Ti_3O_{12}$) to $n = 5$ ($BaLa_4Ti_4O_{15}$) were far more complex. The chemical compositions of these samples can be formulated as $PLa_4Ti_3O_{12} + QBaLa_4Ti_4O_{15}$ or $Ba_QLa_{4(P+Q)}Ti_{3P+4Q}O_{12P+15Q}$. Each expected intergrowth would then consist of the juxtaposition of P perovskite-like blocks $La_4Ti_3O_{12}$ ($n = 4$) and Q perovskite-like blocks $BaLa_4Ti_4O_{15}$ ($n = 5$), and so structurally formulated in compact form, 4^P5^Q. The chemical compositions of the different samples studied and

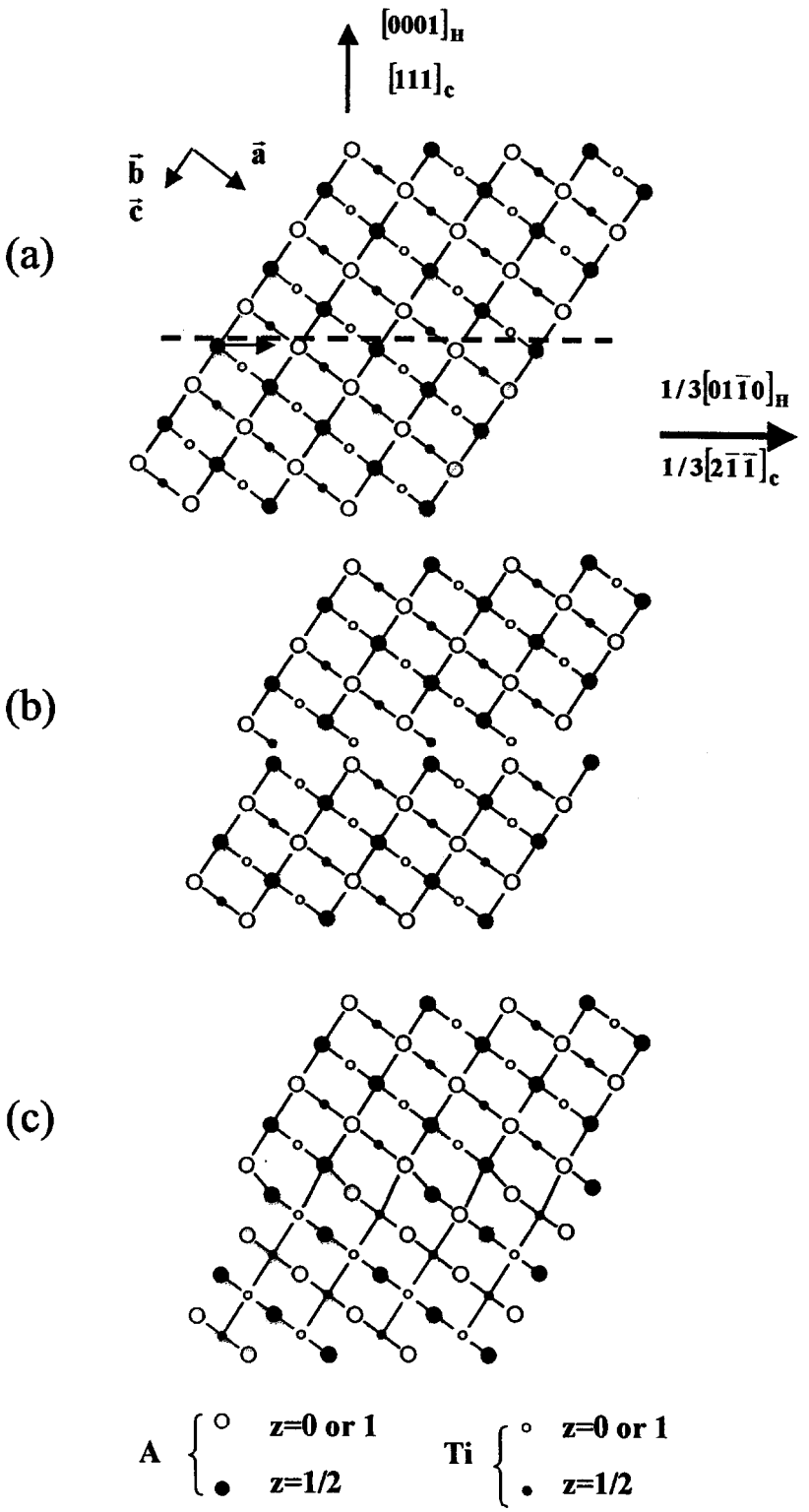

FIG. 4. Schematic diagram illustrating how the bcc cationic subcell characteristic of the perovskite structure is preserved in the $(Ba,La)_nTi_{n-1}O_{3n}$ structures: (a) The bcc cationic subcell of the perovskite structure. (b) The cationic subcell after the 1/3 $[2\bar{1}\bar{1}]_C$ (1/3 $[01\bar{1}0]_H$ shift). (c) The slightly distorted bcc subcell after cation relaxation.

TABLE 3
Relation between Tilting of [TiO_6] Octahedra and Calculated Goldschmit Tolerance Factor t for Some ABO_3 Perovskites and $A_nB_{n-1}O_{3n}$ ($n = 4$, 5, and 6) Cation-Deficient Perovskite-Related Structures ($t = (\langle r_A\rangle + \langle r_O\rangle)/\sqrt{2}(\langle r_B\rangle + \langle r_O\rangle)$ with $\langle r_O\rangle = 1.4$ Å

	Ref.	$\langle r_A\rangle$	$\langle r_B\rangle$	t	Space group	Tilting of [TiO_6] octahedra
$BaTiO_3$	31	1.61	0.605	1.06	$P6_3/mmc$	No
$BaRuO_3$	7	1.61	0.62	1.05	$R\bar{3}m$	No
$Ba_4Nb_2WO_{12}$	10	1.61	0.63	1.05	$R\bar{3}m$	No
Ba_3LaNbO_{12}	10	1.55	0.64	1.03	$R\bar{3}m$	No
$Ba_5Ta_4O_{15}$	11,12	1.61	0.64	1.04	$P\bar{3}m1$	No
$Ba_2La_4Ti_5O_{18}$	25	1.44	0.605	1.00	$R\bar{3}$	No
$BaLa_4Ti_4O_{15}$	26	1.41	0.605	0.99	$P\bar{3}c1$	Yes
$BaLa_4Ti_3RuO_{15}$	14	1.41	0.605	0.99	$P\bar{3}m1$	Yes expected
$La_5Ti_4O_{15}$	5	1.36	0.61	0.97	$P\bar{3}c1$	Yes
$SrLa_4Ti_3RuO_{15}$	14	1.375	0.61	0.98	$P\bar{3}m1$	Yes expected
$SrLa_4Ti_4O_{15}$	4	1.375	0.605	0.98	$P\bar{3}m1$	Yes expected
$CaLa_4Ti_4O_{15}$	4	1.365	0.605	0.98	$P\bar{3}m1$	Yes expected
$La_4Ti_3O_{12}$	This work	1.36	0.605	0.97	$R\bar{3}$	Yes
$CaLa_4Ti_3RuO_{15}$	14	1.356	0.61	0.97	$P\bar{3}m1$	Yes expected
$LaTiO_3$	32	1.36	0.61	0.96	$Pnma$	Yes

the corresponding expected 4^P5^Q intergrowths are given in Table 4. The XRPD patterns are shown in Fig. 5 and call for two main comments:

— All patterns exhibit great analogies.

— Two domains called A (from $La_4Ti_3O_{12}$ up to $BaLa_8Ti_7O_{27}$) and B (from $BaLa_8Ti_7O_{27}$ up to $BaLa_4Ti_4O_{15}$) can, however, be distinguished in Fig. 5 and Table 4. For domain A the pattern profiles are dominated by the $La_4Ti_3O_{12}$ pattern, whereas for domain B they are dominated by the $BaLa_4Ti_4O_{15}$ pattern. In domain A, it is noticeable that some diffraction peaks are slightly and continuously moving in the 2θ position with composition (see arrows in Fig. 5). This behaviour is characteristic of a microphase system. Of course, all attempts to derive unit cell parameters of such microphases were unsuccessful. We therefore had a recourse to high-resolution electron microscopy. Van Tandeloo *et al*., have shown in the case of $La_nTi_{n-\delta}O_{3n}$ microphases (19) that the application of a variant of the "cut and projection" method (30) makes it possible to deduce not only the stacking sequence of microphases but also the main features of their diffraction patterns for given values of n and δ. They also showed that these various stacking sequences could be confirmed and visualized by direct imaging.

The most informative diffraction patterns and high-resolution images are those along the $\langle 01\bar{1}0\rangle_H$ and $\langle 2\bar{1}\bar{1}0\rangle_H$ zone axes (see Figs. 2 and 3). Figures 6 and 7 show the HRTEM images and SAED patterns obtained with the $La_4Ti_3O_{12}$ and $BaLa_4Ti_4O_{15}$ samples, respectively.

On the diffraction patterns, examination of reflections along the c^* direction allows a perfect identification of the stacking sequence:

— The distance between the more intense (basic) spots corresponds to the thickness of an octahedral sheet (≈ 2.2 Å). For example, for $La_4Ti_3O_{12}$ (Fig. 6e) basic spots are the transmitted beam on the one hand and the 00012 reflection on the other hand.

— The number of spots counted from the origin spot to the first basic spot gives the number n of AO_3 layers in a perovskite block.

— The distance between two successive spots corresponds to the thickness of a perovskite block ($\approx n \times 2.2$ Å).

— The l index of the first basic spot gives the total number of AO_3 layers in the unit cell.

High-resolution images obtained along the $\langle 2\bar{1}\bar{1}0\rangle_H$ axes can be interpreted in the light of simulated images calculated for various defocus and sample thickness values. For $La_4Ti_3O_{12}$, exhaustive simulations indicated that the best fit between experimental and calculated images (Fig. 6a) is obtained for a defocus value of -94 nm and for a sample thickness of about 16.5 nm. An enlargement of the calculated image is shown in Fig. 6c. The analysis of the projected potential shown in Fig. 6d clearly reveals that the bright dots correspond to the position of the La columns. By analogy, we suggest that, in all the high-resolution images obtained as well for the two other basic terms (Fig. 7a)

TABLE 4
Chemical Compositions and Expected Intergrowths for the Samples Studied in the $La_4Ti_3O_{12}$–$BaLa_4Ti_4O_{15}$ Domain

Domain	Chemical composition	$La_4Ti_3O_{12}$ mol (P)	$BaLa_4Ti_4O_{15}$ mol (Q)	Expected intergrowth (4^P5^Q)
B	$Ba_6La_{28}Ti_{27}O_{102}$	1	6	(4^15^6)
	$Ba_5La_{24}Ti_{23}O_{87}$	1	5	(4^15^5)
	$Ba_4La_{20}Ti_{19}O_{72}$	1	4	(4^15^4)
	$Ba_3La_{16}Ti_{15}O_{57}$	1	3	(4^15^3)
	$Ba_2La_{12}Ti_{11}O_{42}$	1	2	(4^15^2)
A	$BaLa_8Ti_7O_{27}$	1	1	(4^15^1)
	$BaLa_{12}Ti_{10}O_{39}$	2	1	(4^25^1)
	$BaLa_{16}Ti_{13}O_{51}$	3	1	(4^35^1)
	$BaLa_{20}Ti_{16}O_{63}$	4	1	(4^45^1)
	$BaLa_{24}Ti_{19}O_{75}$	5	1	(4^55^1)
	$BaLa_{28}Ti_{22}O_{87}$	6	1	(4^65^1)
	$BaLa_{32}Ti_{25}O_{99}$	7	1	(4^75^1)
	$BaLa_{36}Ti_{28}O_{111}$	8	1	(4^85^1)
	$BaLa_{40}Ti_{31}O_{123}$	9	1	(4^95^1)
	$BaLa_{44}Ti_{34}O_{135}$	10	1	$(4^{10}5^1)$
	$BaLa_{84}Ti_{64}O_{255}$	20	1	$(4^{20}5^1)$

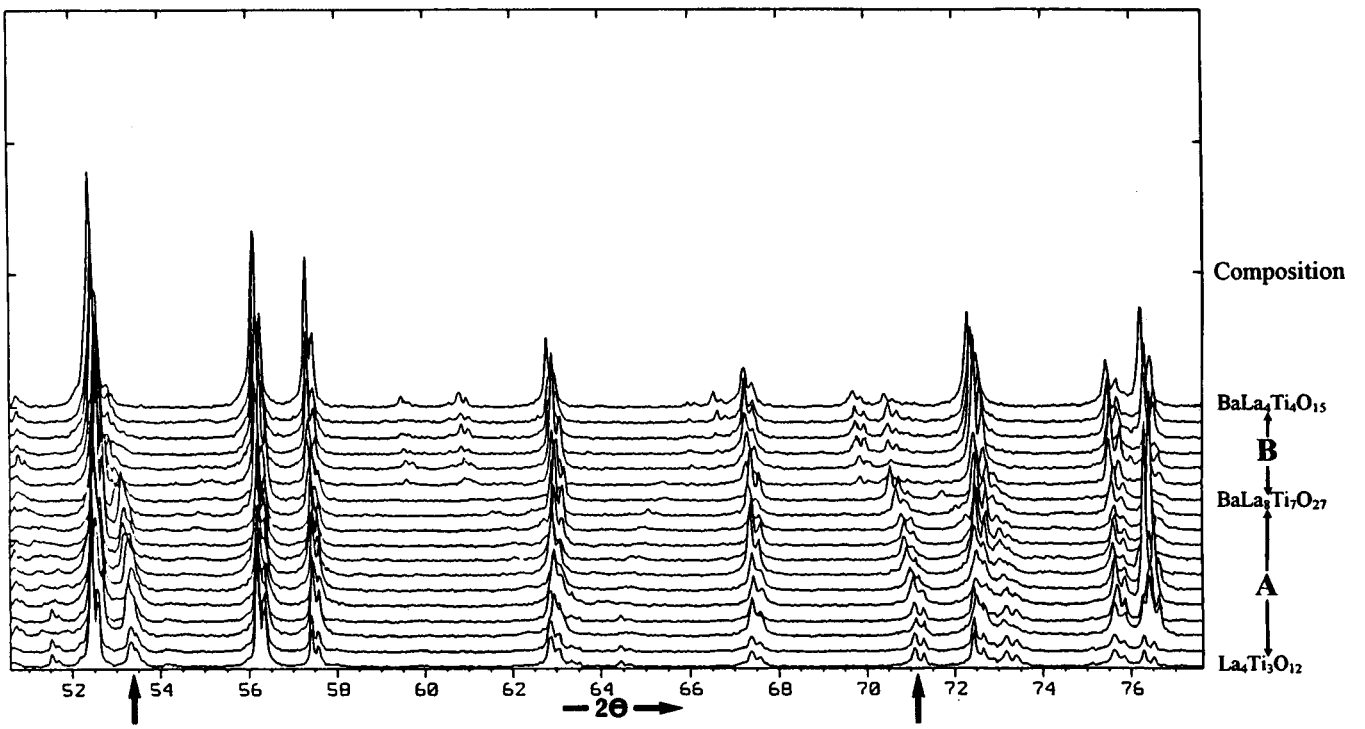

FIG. 5. X-ray diffraction patterns of powder samples reported in Table 4. In the A domain, the arrows indicate the diffraction peaks which are slightly shifted in 2θ in response to chemical changes.

as for the intergrowth sequences (Figs. 8b and 9), this very specific contrast corresponds to the contribution of the A columns. Whereas in the cubic perovskite structure these A-containing columns would form series of straight lines, in the $La_4Ti_3O_{12}$ and $BaLa_4Ti_4O_{15}$ structures they form discontinuous lines because of the periodic $1/3\langle 01\bar{1}0\rangle_H$ shift. The number n of aligned white dots gives the number of AO_3 layers within each perovskite block: $n = 4$ in the case of $La_4Ti_3O_{12}$ and $n = 5$ for $BaLa_4Ti_4O_{15}$. The HRTEM image of Fig. 7a shows that even when the sample is slightly misaligned with the electron beam, the periodicity of the stacking sequence is clearly evidenced.

Figure 8 shows the HRTEM image and the SAED pattern obtained with a crystal of the $BaLa_{16}Ti_{13}O_{51}$ sample. The image confirms the expected ordered intergrowth 4^35^1. The SAED pattern also allows an unambiguous determination of the intergrowth sequence and of the unit cell characteristics. More generally, if we consider a 4^P5^Q sequence, the repeat unit is composed of $n = (4P + 5Q)$ AO_3 layers, of $(n-\delta)$ TiO_6 octahedral sheets, of $\delta = (P + Q)$ perovskite-like blocks respectively characteristic of the two end members and of δ vacancy containing layers. In real space n/δ represents the average spacing between vacancy layers and is equal to the average number of AO_3 layers per perovskite slab ($4 \leq n/\delta \leq 5$). As shown by Van Tandeloo *et al.* (19), in the reciprocal space δ/n corresponds to a modulation vector that determines the separation, along the central diffraction row c^*, of the first relatively intense spot (noted A in Fig. 8a) from the basic spot (noted B in Fig. 8a). As for n, it corresponds to the number of intervals between two basic spots B ($n = 17$ in the pattern of Fig. 8a), whereas δ is the number of intervals counted between an A spot and the closest B spot ($\delta = 4$ in the pattern of Fig. 8a). So an accurate examination of a $[2\bar{1}\bar{1}0]_H$ zone axis pattern provides the

FIG. 6. TEM observations of $La_4Ti_3O_{12}$: (a) HRTEM image obtained along the $[2\bar{1}\bar{1}0]_H$ zone axis. The simulated image (inserted) corresponds to a defocus value of –94 nm and to a thickness of 16.5 nm. The white dots (encircled in the simulated image) are La atoms. (b) Schematic representation of the corresponding structure (Ti atoms are represented by empty circles, Ti-free octahedra by empty squares, and La atoms by filled circles). (c) Enlargement of the calculated image. A schematic projection of the crystalline structure in which only the La atoms are shown (black dots) is inserted. (d) Projected potential reconstructed by crystallographic image processing. The crystalline structure, with unit cell indicated, is superimposed. The smallest points represent oxygen atoms, the medium ones are titanium atoms, and the big black dots represent the lanthanum. (e) $[2\bar{1}\bar{1}0]_H$ zone axis diffraction pattern. (f) $[01\bar{1}0]_H$ zone axis diffraction pattern.

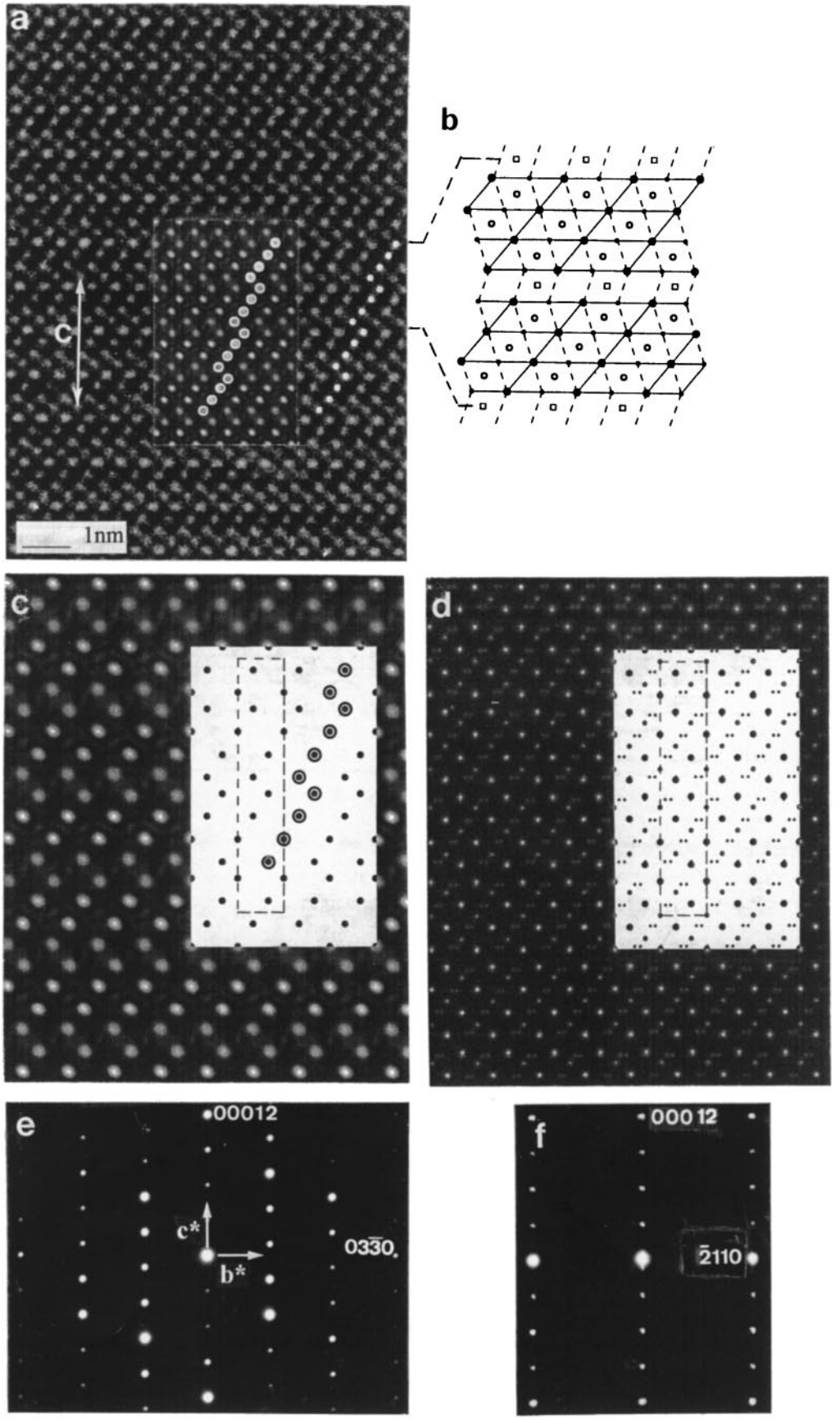
a
c
1nm
b
c
d
e
00012
c*
b*
03$\bar{3}$0
f
00012
$\bar{2}$110

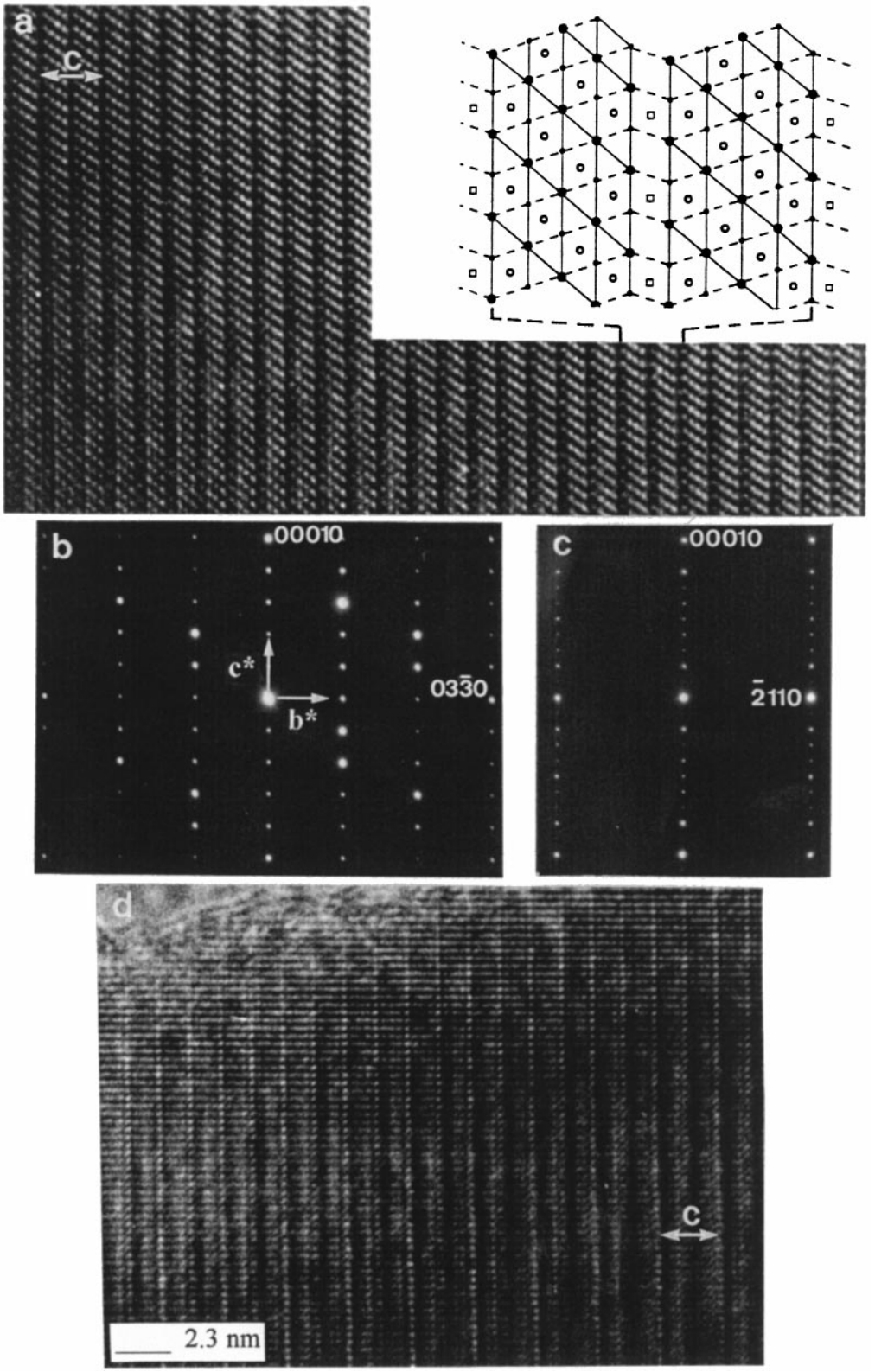

FIG. 7. TEM observations of $BaLa_4Ti_4O_{15}$: (a) HRTEM image obtained along the $[2\bar{1}\bar{1}0]_H$ zone axis and the schematic representation of the corresponding structure (Ti atoms are represented by empty circles, Ti-free octahedra by empty squares, and La atoms by filled circles). (b) $[2\bar{1}\bar{1}0]_H$ zone axis diffraction pattern. (c) $[0\bar{1}\bar{1}0]_H$ zone axis diffraction pattern. (d) HRTEM image obtained along the $[01\bar{1}0]_H$ zone axis, showing the doubling of the *c* parameter.

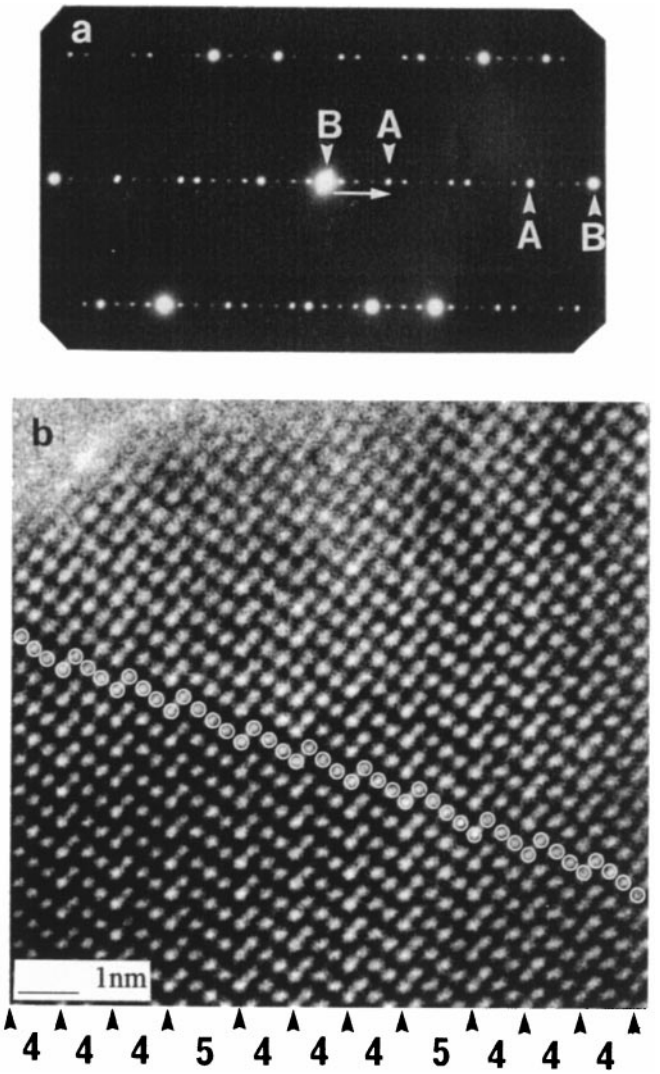

FIG. 8. TEM observations of $BaLa_{16}Ti_{13}O_{51}$: (a) SAED pattern with $[2\bar{1}\bar{1}0]_H$ zone axis. (b) HRTEM image obtained along the $[2\bar{1}\bar{1}0]_H$ zone axis which visualizes the ordered 4^35^1 intergrowth.

necessary information to establish the P and Q values of any 4^P5^Q intergrowth sequence. For each microphase, the characteristic 4^P5^Q sequence corresponds to a repeat unit along the c axis. Indeed, for a general model, the determination of the c parameter of the different microphases requires one to take into account the two following points.

First, the Bravais lattice of the structure is determined by the number n of AO_3 layers in the 4^P5^Q repeat unit. As was the case for the simple terms of the $A_nB_{n-1}O_{3n}$ series (see the beginning of the second section), when n is a multiple of 3 or a multiple of 3 $+1$, the Bravais lattice is R and the periodicity along c requires three 4^P5^Q repeat units.

Second, because of the rotation of the octahedra within the $BaLa_4Ti_4O_{15}$ perovskite blocks (see the end of the second section), the number of these blocks in the unit cell for any microphase has to be even.

These two conditions result in complex intergrowths involving various numbers of 4^P5^Q repeat units.

As an example, consider a series for which $Q = 1$ (4^P5^1 intergrowth terms; see Table 5),

— When P is a multiple of 3 (4^35^1 or 4^65^1 intergrowths, for example), n is obviously a multiple of 3 -1, and the lattice parameter is twice the thickness of the repeat unit and the lattice mode is P (H polytypoid). For 4^35^1 intergrowth, for example, the unit cell contains $2 \times n = 34$ AO_3 layers, the lattice mode is P and the full stacking sequence corresponds to Scheme 1.

— When P is not a multiple of 3 (4^25^1 or 4^45^1 intergrowths, for example), n is a multiple of 3 or 3 $+1$, and the lattice parameter is 6 times the thickness of the repeat unit. The resulting structure is rhombohedral (R mode). For example, for the 4^15^1 microphase the stacking of the 54 AO_3 layers corresponds to Scheme 2, and the lattice mode is R.

The Observed Intergrowths

TEM observations were carefully carried out on all the samples reported in Table 4. They confirmed the separation in two domains indicated by the previous XRD study.

Domain A. For all the samples of this domain, perfectly ordered intergrowths were observed. As clearly indicated by both HRTEM images (Fig. 9) and SAED patterns (Fig. 10) only 4^P5^1 sequences could be synthesized.

The ease of obtaining them is strongly dependent on their chemical composition: the simplest 4^15^1 intergrowth is seldom observed even after very long annealing (72 h) at high temperature (1600°C), whereas the more complex 4^45^1 and particularly 4^35^1 sequences are easily formed. The percentage of ordered parts of crystals, roughly estimated on the basis of a statistical TEM approach, is 5% for $P = 1$, 20% for $P = 2$, 40% for $P = 5$, 70% for $P = 4$, and 90% for $P = 3$. For samples with a composition corresponding to higher P values ($P > 6$) long-range ordering is very difficult to reach. However, after three successive thermal treatments

/$\underline{A}$BCA/CABC/BCAB/ABCAB/A′B′C′A′/C′A′B′C′/B′C′A′B′/A′B′C′A′B′/$\underline{A}$

4a 4a 4a 5a 4b 4b 4b 5b

SCHEME 1

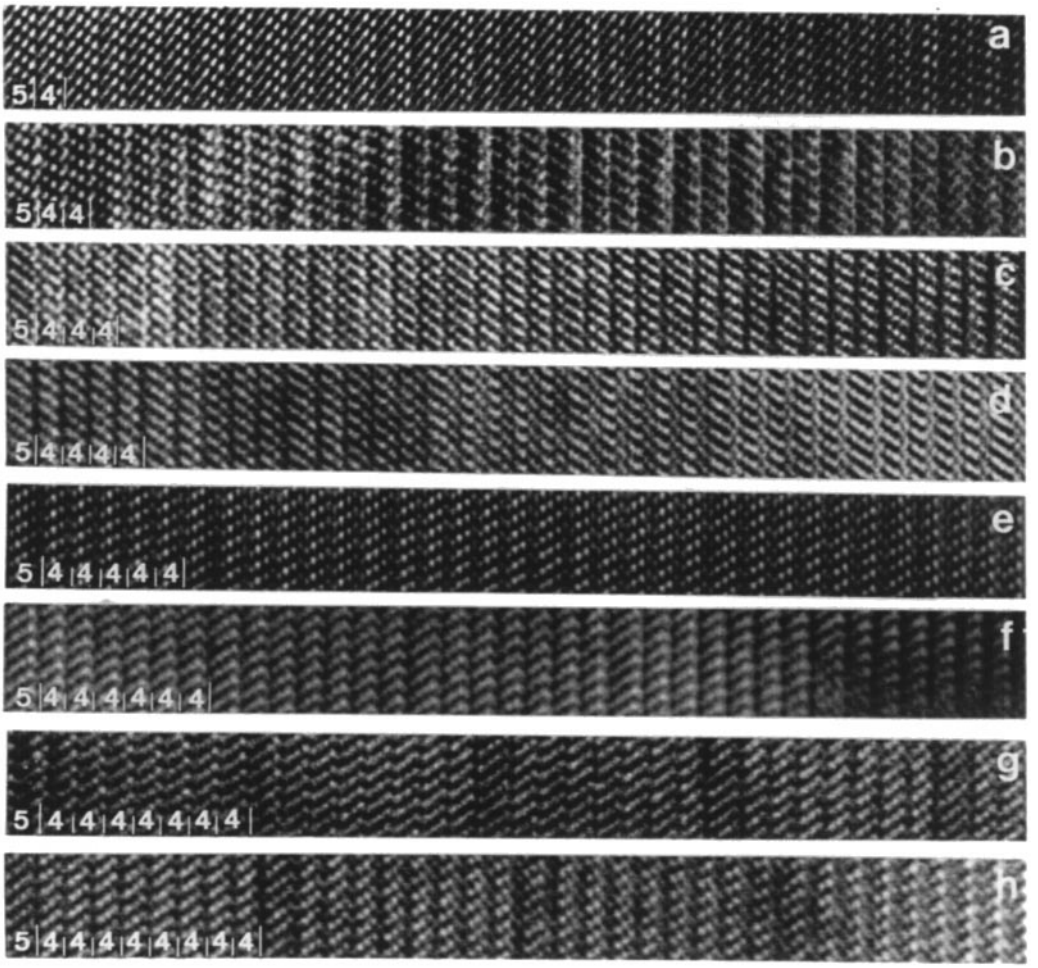

FIG. 9. HRTEM image obtained along the $[2\bar{1}\bar{1}0]_H$ zone axis for different microphases: (a) $BaLa_8Ti_7O_{27}$: 4^15^1. (b) $BaLa_{12}Ti_{10}O_{39}$: 4^25^1. (c) $BaLa_{16}Ti_{13}O_{51}$: 4^35^1. (d) $BaLa_{20}Ti_{16}O_{63}$: 4^45^1. (e) $BaLa_{24}Ti_{19}O_{75}$: 4^55^1. (f) $BaLa_{28}Ti_{22}O_{87}$: 4^65^1. (g) $BaLa_{32}Ti_{25}O_{99}$: 4^75^1. (h) $BaLa_{36}Ti_{28}O_{111}$: 4^85^1.

of 24 h at respectively 1620, 1630, and 1640°C, interspersed by a meticulous grinding of the samples, extended domains of ordered 4^75^1 and 4^85^1 sequences could be observed. The corresponding images are shown in Figs. 9g and 9h. Nevertheless, these samples are not ordered enough to produce coherent and representative SAED patterns. The main structural characteristics of the observed microphases are reported in Table 5.

Domain B. In contrast to domain A none of the expected ordered sequences in domain B indicated in Table 4 could be observed, despite a very long time of annealing at high temperatures of the corresponding samples. Most of the samples display crystalline areas characterized by 4^P5^1 sequences (mainly 4^35^1 and 4^45^1) together with large domains of $BaLa_4Ti_4O_{15}$, the simple term (5^1). These observations are in agreement with the previous XRD study. Indeed, as shown in Fig. 5 the B domain is mainly dominated by the diffraction pattern of the $BaLa_4Ti_4O_{15}$ member. The TEM investigation confirms that no long-range ordered 4^P5^Q intergrowth can be formed when Q is higher than 1.

/ABCA/CABCA/C′A′B′C′/B′C′A′B′C′/BCAB/ABCAB/A′B′C′A′/C′A′B′C′A′/CABC/BCABC/B′C′A′B′/A′B′C′A′B′/A

4a 5a 4b 5b 4a 5a 4b 5b 4a 5a 4b 5b

1 **2** **3**

SCHEME 2

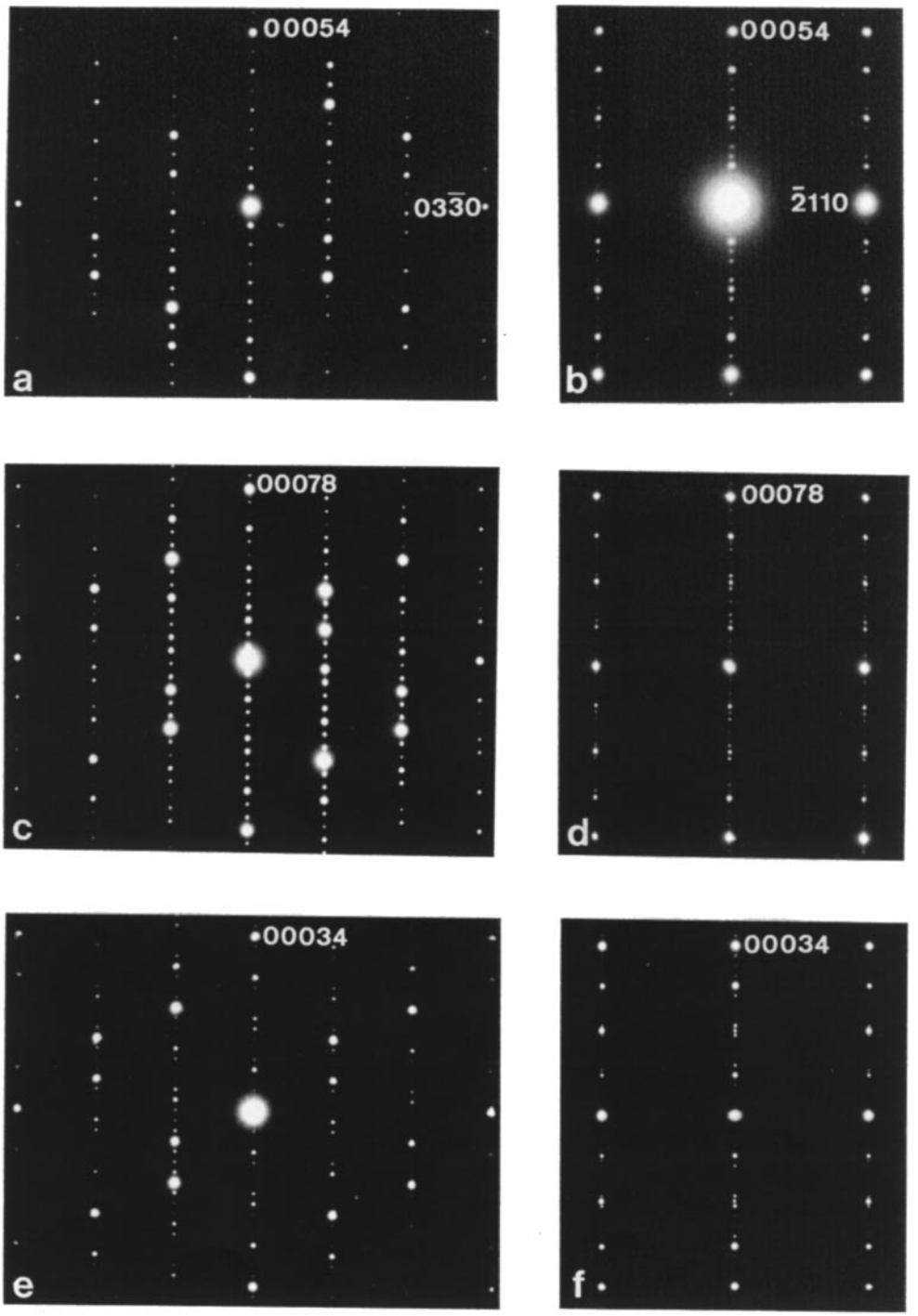

FIG. 10. SAED pattern for different microphases: (a) and (b): $[2\bar{1}\bar{1}0]_H$ and $[01\bar{1}0]_H$ zone axis patterns of a 4^15^1 intergrowth. (c) and (d): $[2\bar{1}\bar{1}0]_H$ and $[01\bar{1}0]_H$ zone axis patterns of a 4^25^1 intergrowth. (e) and (f): $[2\bar{1}\bar{1}0]_H$ and $[01\bar{1}0]_H$ zone axis patterns of a 4^35^1 intergrowth. (g) and (h): $[2\bar{1}\bar{1}0]_H$ and $[01\bar{1}0]_H$ zone axis patterns of a 4^45^1 intergrowth. (i) and (j): $[2\bar{1}\bar{1}0]_H$ and $[01\bar{1}0]_H$ zone axis patterns of a 4^55^1 intergrowth. (k) and (l): $[2\bar{1}\bar{1}0]_H$ and $[01\bar{1}0]_H$ zone axis patterns of a 4^65^1 intergrowth.

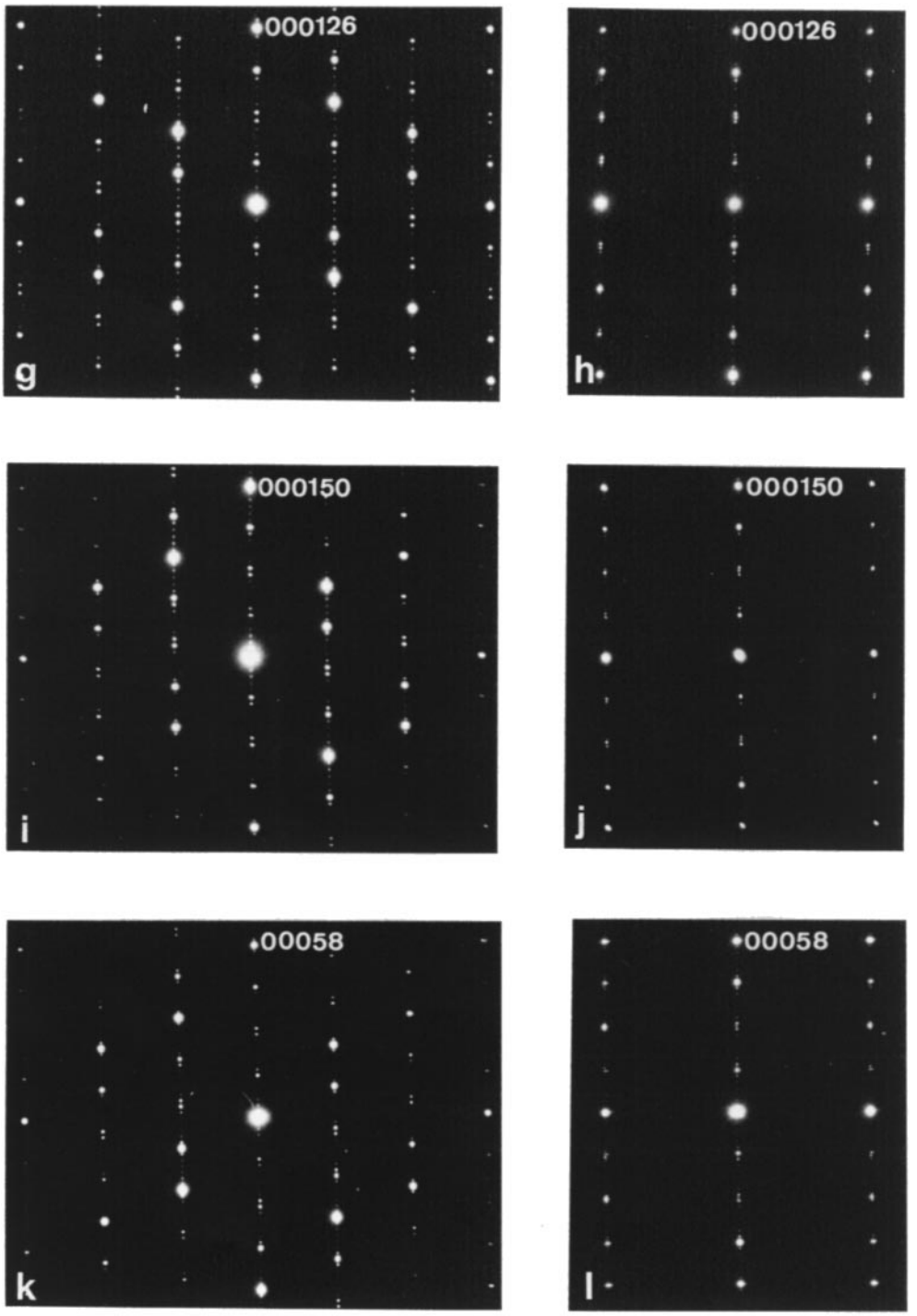

FIGURE 10—*Continued*

DISCUSSION AND CONCLUSIONS

In the present study we have shown that in the part of the $La_4Ti_3O_{12}$–$BaTiO_3$ system not yet investigated (see Fig. 1), the large nonstoichiometric domain observed can be justified by the formation of a continuous series of complex microphases which correspond to coherent intergrowths of the $La_4Ti_3O_{12}$ and $BaLa_4Ti_4O_{15}$ members. All the observed sequences are uniform and thus produce sharp diffraction spots. They all correspond to the general formula

TABLE 5
Structural Characteristics of the 4^P5^1 Microphases

Chemical composition of samples	$BaLa_8Ti_7O_{27}$	$BaLa_{12}Ti_{10}O_{39}$	$BaLa_{16}Ti_{13}O_{51}$	$BaLa_{20}Ti_{16}O_{63}$	$BaLa_{24}Ti_{19}O_{75}$	$BaLa_{28}Ti_{22}O_{87}$
Results of the electron diffraction study						
n	9	13	17	21	25	29
δ	2	3	4	5	6	7
P	1	2	3	4	5	6
Q	1	1	1	1	1	1
(4^P5^Q) intergrowth observed	(4^15^1)	(4^25^1)	(4^35^1)	(4^45^1)	(4^55^1)	(4^65^1)
⇓	⇓	⇓	⇓	⇓	⇓	⇓
Resulting chemical composition:	$BaLa_8Ti_7O_{27}$	$BaLa_{12}Ti_{10}O_{39}$	$BaLa_{16}Ti_{13}O_{51}$	$BaLa_{20}Ti_{16}O_{63}$	$BaLa_{24}Ti_{19}O_{75}$	$BaLa_{28}Ti_{22}O_{87}$
Structural characteristics						
Thickness of a 4^P5^Q sequence (nm)	1.99	2.85	3.71	4.52	5.46	6.33
Lattice mode	R	R	P	R	R	P
Number of 4^P5^Q sequences per unit cell	6	6	2	6	6	2
Number of AO_3 planes per unit cell	54	78	34	126	150	58
Polytypoid	54R	78R	34H	126R	150R	58H
c-parameter (nm)	11.94	17.14	7.42	27.15	32.74	12.66

$Ba_QLa_{4(P+Q)}Ti_{3P+4Q}O_{12P+15Q}$ and can be denoted, in a compact form, by 4^P5^Q, but only those corresponding to $Q = 1$ seem to be stable (Table 5). In domain B, for which 4^15^Q intergrowths could be expected, it is mainly the most stable 4^35^1 intergrowth which is observed together with $BaLa_4Ti_4O_{15}$ (5^1). Moreover, for compositions ranging from $BaLa_8Ti_7O_{27}$ (4^15^1) to $La_4Ti_3O_{12}$ (4^1), 5^2 sequences are never observed, even for complex intergrowths for which various distributions of the P La_4TiO_{12} and Q $BaLa_4Ti_4O_{15}$ blocks are possible. For example, with a $Ba_2La_{36}Ti_{29}O_{114}$ sample, which corresponds to a half and half mixture of the $BaLa_{16}Ti_{13}O_{51}$ and $BaLa_{20}Ti_{16}O_{63}$ compounds (see Table 4), in principle 4^75^2 as well as $4^35^14^45^1$ sequences could be expected. It is systematically the latter which is observed (Fig. 11) and complex intergrowths of different 4^P5^1 sequences are preferentially developed. Such observations can be easily justified if we consider that the absence of titanium cations along the interfaces (i.e., at the center of the hcp part of these superstructures) leads to a repulsive Coulomb-type interaction between successive parallel interfaces. Van Tandeloo *et al.* (19) have shown that the best configuration for a set of parallel interfaces, interacting by repulsive forces, is the equidistant arrangement. Therefore, it is evident that the intercalation of $BaLa_4Ti_4O_{15}$ perovskite blocks (5^1) between several La_4TiO_{12} blocks (4^1) is, in contrast to the reverse process, a stabilizing factor. Moreover, it obviously allows a more uniform (equidistant) distribution of both interfaces and perovskite blocks with opposite octahedra tilting (blocks noted (BCABC) and (B′C′A′B′C′) in Fig. 3b).

In agreement with the observations of Saltykova *et al.* (1), no 5^P6^Q intergrowths were observed in the $Ba_2La_4Ti_5O_{18}$–$BaLa_4Ti_4O_{15}$ part of the diagram (Fig. 1). A comparison of the crystal structure of these two basic members could provide a reasonable explanation for this phenomenon. In

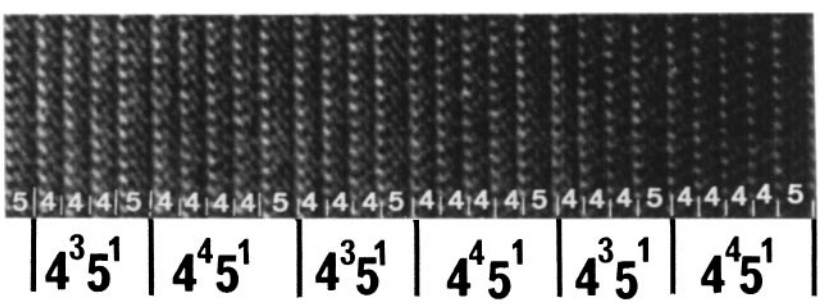

FIG. 11. HRTEM image obtained along the $[2\bar{1}\bar{1}0]_H$ zone axis of a crystal displaying a complex and well-ordered intergrowth based on the combination of 4^35^1 and of 4^45^1 intergrowth terms.

fact, in the $Ba_2La_4Ti_5O_{18}$ structure, the quantity of La atoms is not sufficient to induce any rotation of TiO_6 octahedral within the perovskite blocks. Therefore, each possible 5^p6^Q intergrowth would lead to small misfits between the distorted AO_3 layers at the interfaces of the $BaLa_4Ti_4O_{15}$ perovskite blocks and the undistorted AO_3 layers of the $Ba_2La_4Ti_5O_{18}$ perovskite blocks. The corresponding strains induced could thus destabilize the structure. It could be interesting, from this point of view, to try to see what really happens at high temperature in the $Ba_4La_4Ti_7O_{24}$–$Ba_2La_4Ti_5O_{18}$ part of the system and also to study the $SrTiO_3$–La_4TiO_{12} system, for which all basic members are expected to present undistorted perovskite-like blocks. This will be the subject of forthcoming studies.

REFERENCES

1. V. A. Saltykova, O. V. Mel'nikova, N. V. Leonova, and N. F. Fedorov, *Russ. J. Inorg. Chem.* **30**(1), 105 (1985).
2. N. F. Federov, O. V. Mel'nikova, V. A. Saltykova, and M. V. Chistykova, *Russ. J. Inorg. Chem.* **24**(5), 649 (1979).
3. M. German and L. M. Kovba, *Russ. J. Inorg. Chem.* **28**(9), 2377 (1983).
4. M. German and L. M. Kovba, *Russ. J. Inorg. Chem.* **30**(2), 317 (1985).
5. R. Bontchev, B. Darriet, J. Darriet, and F. Weill, *Eur. J. Solid State Inorg. Chem.* **30,** 273 (1993).
6. C. Calvo, H. N. Ng, and B. L. Chamberland, *Inorg. Chem.* **17**(3), 696 (1978).
7. P. C. Donohue, L. Katz, and R. Ward, *Inorg. Chem.* **4**(3), 306 (1965).
8. J. M. Longo, L. Katz, and R. Ward, *Inorg. Chem.* **4**(2), 235 (1965).
9. S. Kemmler-Sack, *Z. Anorg. Allg. Chem.* **457,** 157 (1979).
10. H. J. Von Rother, S. Kemmler-Sack, U. Treiber, and W. R. Cyris, *Z. Anorg. Allg. Chem.* **466,** 131 (1980).
11. F. Galasso and L. Katz, *Acta Crystallogr.* **14,** 647 (1961).
12. J. Shannon and L. Katz, *Acta Crystallogr. B* **26,** 102 (1970).
13. J. L. Hutchison and A. J. Jacobson, *J. Solid State Chem.* **20,** 417 (1977).
14. R. Bontchev, F. Weill,and J. Darriet, *Mater. Res. Bull.* **27,** 931 (1992).
15. R. Bontchev, B. Darriet, J. Darriet, F. Weill, G. Van Tendeloo, and S. Amelincks, *Eur. J. Solid State Chem.* **30**(5), 521 (1993).
16. W. Wischert, H. J. Schittenhelm, and S. Kemmler-Sack, *Z. Anorg. Allg. Chem.* **439,** 250 (1978).
17. W. Wischert, H. J. Schittenhelm, and S. Kemmler-Sack, *Z. Anorg. Allg. Chem.* **448,** 119 (1979).
18. V. A. Saltykova, O. V. Mel'Nikova, and N. F. Fedorov, *Russ. J. Inorg. Chem.* **34**(5), 758 (1989).
19. G. Van Tendeloo, S. Amelinx, B. Darriet, R. Bontchev, J. Darriet, and F. Weill, *J. Solid State Chem.* **108,** 314 (1994).
20. S. Kemmler-Sack and U. Treiber, *Z. Anorg. Allg. Chem.* **462,** 166 (1980).
21. S. Kemmler-Sack, *Z Anorg. Allg. Chem.* **461,** 146 (1980).
22. D. Pasero and R. J. D. Tilley, *J. Solid State Chem.* **135,** 260 (1998).
23. N. Harre, Thesis, University of Limoges, France, 1996.
24. N. Harre, D. Mercurio, G. Trolliard, and J. P. Mercurio, *Ann. Chim. Sci. Mater.* **23,** 233 (1998).
25. N. Harre, D. Mercurio, G. Trolliard, and B. Frit, *Eur. J. Solid State Inorg. Chem.* **35,** 77 (1998).
26. N. Harre, D. Mercurio, G. Trolliard, and B. Frit, *Mater. Res. Bull.* **33(10),** 1537 (1998).
27. A. M. Glazer, *Acta Crystallogr. Sect. B* **28,** 3384 (1972).
28. V. M. Goldschmidt, *Naturwissenschaften* **14,** 477 (1926).
29. P. A. Stadelmann, *Ultramicroscopy* **21,** 131 (1987).
30. V. Elser, *Phys. Rev. B* **32,** 4892 (1985), *Acta Crystallogr. Sect. A* **42,** 36 (1986).
31. J. Akimoto, Y. Gotoh, and Y. Oosawa, *Acta Crystallogr. Sect. C* **50,** 160 (1994).
32. M. Eitel and J. E. Greedan, *J. Less-Common Met.* **116,** 95 (1986).